Empirical Estimation of Intra-Voxel Structure with Persistent Angular Structure and Q-ball Models of Diffusion Weighted MRI

By

Vishwesh Nath

Thesis

Submitted to the Faculty of the

Graduate School of Vanderbilt University

in partial fulfillment of the requirements

for the degree, of

Master of Science

in

Computer Science

May, 2017

Approved:

Bennett A. Landman, Ph.D.

Richard A. Peters, Ph.D.

Dedication

To my parents Justice Vikram Nath and Dr. Sangita Srivastava who gave birth to this possibility.

To my second set of parents Jared Watson and Nina Watson.

My Research Advisor and Mentor Dr. Landman. This would not have been possible without his support.

Last but not the least friends: Ayan, Amogh & Chandan. My partners in mischief.

Acknowledgements

Table of Contents

List of Figures

Chapter 1

Introduction

Diffusion weighted magnetic resonance imaging (MRI) enables non-invasive milli-metric mapping of local tissue orientation via sensitivity to directional diffusion on the micrometer scale. The tensor model in diffusion tensor imaging (DTI) has been wildly successful for interpreting this signal in cerebral white matter tracts and reconstructing major fiber pathways in the brain as it is sensitive to fiber orientations [1]. To address DTI's shortcomings in regions of complex intra-voxel structure, High Angular Resolution Diffusion Imaging (HARDI) methods acquir and analyze additional data to estimate multiple fiber population orientations per voxel. These methods reveal more elaborate information about the intra-voxel structure, e.g., Diffusion Orientation Transform (DOT) [2], Spherical Deconvolution (SD) [3, 4], Persistent Angular Structure (PAS-MRI) [5] or Q-ball [6].

Previous large scale reproducibility studies with DTI have been essential for understanding the empirical behavior of the tensor estimator (e.g., [7]). Yet, the bias and variance of HARDI methods has not been as well characterized empirically. To address this shortcoming, we perform an in-depth comparison of PAS-MRI and Q-ball as representative variants of HARDI methods. PAS-MRI models the intra-voxel diffusion using a discrete number of fiber compartments [8], while Q-ball estimates an orientation distribution function (ODF), which is assumed to reflect the underlying fiber orientation distribution through its impact on diffusivity [9]. PAS has been shown to be more consistent than Q-ball on synthetic data at lower or clinical b-values of about 1200 s/mm^2 [8, 10]. Meanwhile, Q-ball is effective at higher b-values (~3000 s/mm^2 or greater) [6]. Previous work on Q-ball has also shown that it resolves multiple fiber orientations for fractional anisotropy (FA) regions < 0.4 [11]. While a minimum angle of fiber orientations has not been established for PAS yet, Q-ball has been known to resolve angles down to 45 degrees with diminishing accuracy depending on adequate signal to noise ratio (SNR) [12]. Herein, we compare the empirical reproducibility of PAS-MRI and Q-ball focusing on b-values of 1000 and 3000 s/mm^2. We have also compared across the models in terms of agreement between PAS & Q-ball.

Chapter 2

Methods

Briefly, the data were pre-processed for each scan session individually and successively registered to the Montreal Neurological Institute (MNI) space template (Figure 1). Gold standard models were created for each method and b-value by concatenating the 11 scans per b-value and fitting with each method. Comparisons were performed across repetitions to assess variance/reproducibility, while comparisons between the gold standard scans were performed to assess bias.

2.1 DW-MRI Data Measurements

A healthy volunteer was scanned in three different sessions on successive days on a 3T Phillips Scanner with a 32-channel head coil. The first and last scan sessions consisted of four repetitions of 96 gradient directions per b-values at each of 1000 and 3000 s/mm^2. The second session had three repetitions of as per the mentioned protocol. For each b-value shell, ten minimally weighted reference images (b0's) were also acquired. Voxel resolution for the data is 2.5mm x 2.5mm x 2.5mm with a matrix of 96 x 96 and 38 slices. The scan parameters were: Multi-Band=2; SENSE=2.2; TR= 2650 ms; TE=94 ms; partial Fourier=0.7. Fold over direction was A-P with a P fat shift. For each set of 5 shells, an additional diffusion scan was acquired with reverse phase encoded volumes (i.e., fold over direction A-P with A fat shift) with a minimally weighted volume and 3 diffusion weighting directions with a b-value of 1000 s/mm^2 along the imaging frame cardinal directions, and all other parameters were kept constant.

2.2 Data Pre-processing

Each session was corrected for eddy current motion, patient head movement and susceptibility distortion with FSL's topup and eddy [13, 14]. Every diffusion weighted shell was preceded by a non-diffusion weighted image (b0) averaged ten times on the scanner, and each session had four reverse phase encoded b0 volumes. All b0's including reverse phase encoded b0's in a session were concatenated and fed as inputs to topup. For eddy all scans in a session were concatenated and then corrected together using the results from topup). Once topup and eddy had been performed the corrected b0's from the first session were registered to a 2.5mm isotropic MNI T2 which was resampled from a 0.5mm weighted template using six degree of

freedom registration [15]. The volumes for the next session were brought to the same space by averaging the b0's together and registering the combined image to the averaged b0's in the first session. The same procedure was subsequently done to the last session to bring all three sessions into a common subject-specific pose aligned with MNI space.

Thereafter, all the sessions were normalized by the b0 corresponding to the scan to account for amplitude drift (**Figure 1**). A weighted mean b0 was created from all b0 scans in MNI space by a weighted average of all b0's. The weight was taken as the inverse of the median of all b0 scans in MNI space averaged with the mean of b0's from all sessions. The final normalization scan was computed by multiplying the weighted mean b0 to the ratio of diffusion weighted scan (in MNI space) to the b0 (in MNI space).
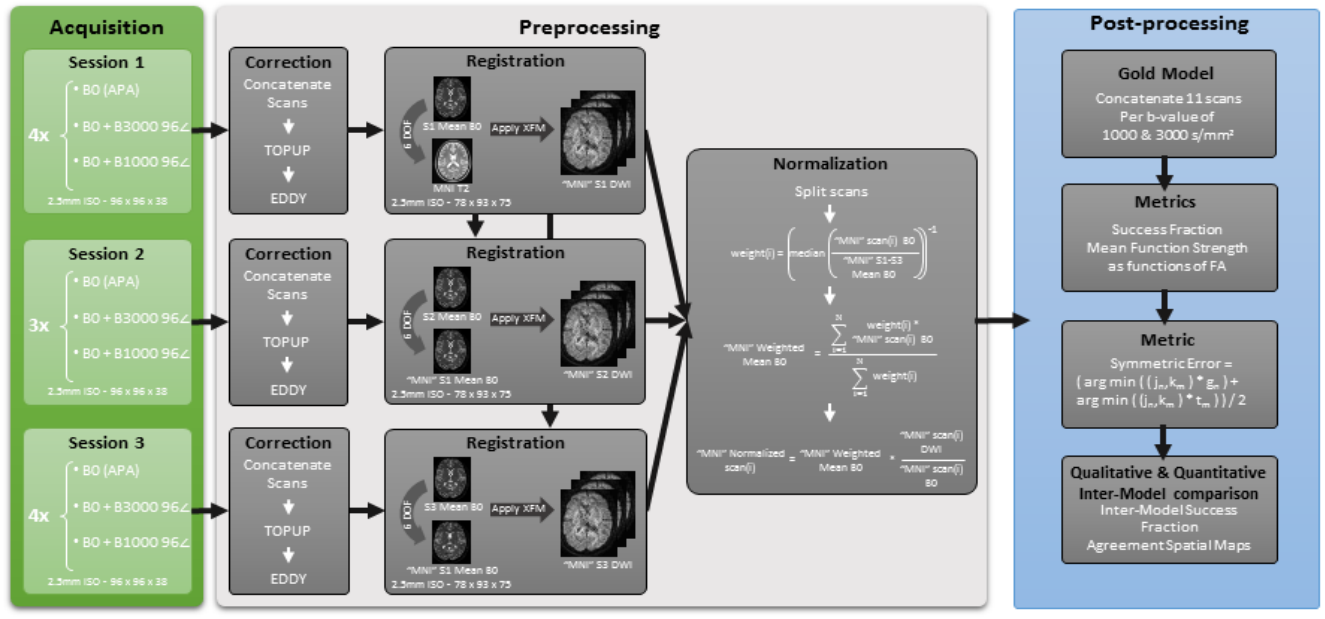
Figure 1: Flowchart depicting the pipeline of data processing steps.

2. 3 Data Segmentation

Individual target images (T1 weighted scans) were affine registered to the MNI305 atlas [16] and bias corrected with N4 [17] using Advanced Normalization Tools (ANTs)[18] on the atlas and the target images. Non-rigid registration was performed from atlas images to the target image using Advanced Normalization Tools (ANTs) and symmetric image normalization algorithm (SyN)[19]. Image and label volumes for the atlas were then deformed to the target space with bi-cubic and nearest-neighbor interpolation and fused with non-local spatial STAPLE

3

[20, 21] and Adaboost correction [22]. Each individual voxel in the brain was labelled to one of the 133 labels obtained from the multi-atlas labelling using the BrainCOLOR protocol [23]. T1 image labels were brought back to original target space with the ANTs inverse transformation. All WM labels were concatenated together to create a WM mask. The mask has been used for all reported results with the only exception of the visual glyphs where we have shown all data for the particular slice.

2.4 Q-ball Reconstruction

Q-ball was reconstructed following [9] in the Camino toolkit [24, 25] using Spherical Harmonic Basis Functions with an order 8 for basis as per guidance in [9].

2.5 RE-PASMRI Reconstruction

PAS was reconstructed from maximum entropy spherical deconvolution [26] with the reduced encoding model [8] with a reduction factor of 16. The gold standard sets of the PAS were computed in an "embarrassingly parallel" computation model (split across axis stacks) across multiple CPU's so as not to affect the algorithm in anyway but ensure computation at reasonable speeds.

2.6 Peak Reconstruction

The peak reconstruction of the ODF and the PAS was performed using sfpeaks from Camino which is an implementation for searching the local maxima of the reconstructed PAS and ODF's using Powell's method [5].

Chapter 3

Metrics

3.1 Success Fraction

Success fraction (SF) has been effectively applied to characterize synthesized data on a small scale in vivo dataset [10], originally termed as consistency fraction in the article. Success fraction declares two intra-voxel measurements to be in agreement if (1) the number of fiber populations is equivalent and (2) the peaks are within an angular tolerance. In [10], 18 degrees was used as the tolerance; herein we use 20 degrees.

All metrics have been binned at intervals of 0.1 by FA. The binned values have been represented by the mean with standard deviations across the bin.

3.2 Peak Fraction

The peak fraction is a representation of the function value detected from the PAS or the ODF. We have restricted the analysis to scenarios of $<= 3$ fiber populations per voxel and that had been defined during the peak search algorithms as well. The ODF/PAS values were normalized in cases where fiber populations detected were > 1. It has been defined as a function of FA and is also mapped to the number of voxels. We have chosen to represent this for all the eleven single test models per b-value for both the methods, where f_i^n are the normalized peak fraction (PAS/ODF) values of the peaks detected and f_i is the function value (PAS/ODF) of the peak detected:

$$f_i^n = f_i / (f_1 + f_2 + f_3) \qquad (1)$$

3.3 Symmetric Angular Error

Symmetric angular error presents an insight to bias of the reproducibility of the fiber populations being detected from the PAS and Q-ball functions and a different perspective from the SF as it combines it with quantitative peak fractions. It informs us about quantitative error presence even in cases where the gold standard model detects two populations and the test model detects three. Consider two vectors, a gold standard vector, j_n, and test model vectors, k_m, along with gold

standard weights, g_n, and test weights, t_m. The symmetric angular error (SAE) is a representation of the orientation error between all the peaks of the gold model and the test model:

$$(\arg\min(\sphericalangle(j_n, k_m) * g_n) + \arg\min(\sphericalangle(j_n, k_m) * t_m)) / 2 \quad (2)$$
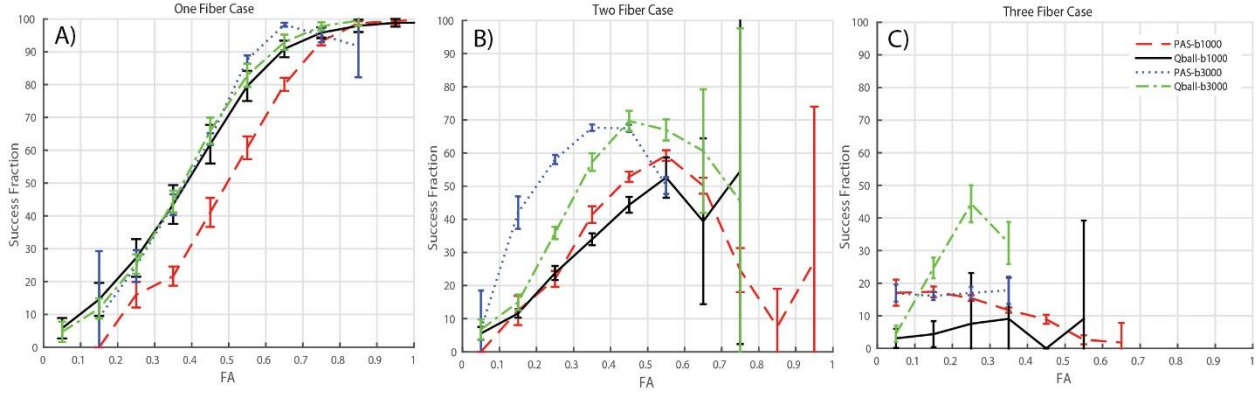

Figure 2: SF separated in fiber population cases from PAS and Q-ball at b-values of 1000 s/mm^2 and 3000 s/mm^2. A) Single fiber population detected by gold standard methods. B) Two fiber population detected by gold standard methods. C) Three fiber population detected by gold standard methods.

Chapter 4

Results

With the one-fiber case, SF for PAS and Q-ball shows increasing consistency as a function of FA (Figure 2A). It should be noted that SF for PAS at a b-value of 1000 s/mm^2 is significantly lower. At the extremes of FA (0.8-0.9 or 0.1-0.2), limited sample sizes lead to higher variance in the estimates (e.g., PAS at a b-value of 3000 s/mm^2). With the two-fiber case (Figure 2B), SF is maximal at intermediate FA (0.35-0.55 PAS and ~0.55 for Q-ball). With the three-fiber case, SF is generally low for both methods while Q-ball at a b-value of 3000 s/mm^2 shows the highest SF.

Figure 3 explores both the number of voxels identified along with the FA, and peak fraction. Q-ball shows more voxels with single fiber populations than PAS at both b-values (Figure 3A). As the b-values increase, PAS exhibits a slight increase in the single fiber voxels while Q-ball finds a substantial decrease. With the two-fiber case, PAS estimates a wide spread of peak fraction (0.5-0.8) for a range of FA (0.2-0.8), but Q-ball finds a very narrow, peak fraction of (0.5-0.6) for a more limited range of FA (0.3-0.6). The number of two-fiber voxels moderately increases with b-value for PAS and Q-ball. For the three-fiber case, there is substantial decrease in detected fibers with PAS, but an increase with Q-ball. For a b-value of 1000 s/mm^2, PAS finds 3 fibers for an FA of 0-0.6, but for a b-value of 3000 s/mm^2, PAS detects 3 fibers only FA < 0.4. For Q-ball, the FA range remains the same (FA in 0-0.5) with a peak fraction of ~one third for both b-values.

The single fiber cases exhibit symmetric angular error less than multi-fiber cases for both PAS and Q-ball (Figure 4). Symmetric angular error decreases with increased FA for all scenarios. PAS shows lower symmetric angular error than Q-ball (Figure 4A vs. 4B and Figure 4C vs. 4D). Interestingly, symmetric angular errors are lower for the three crossing fibers relative to the two crossing fibers. Yet, note that 7836 and 661 voxels were detected with three fibers for PAS and Q-ball at b-value of 1000 s/mm^2 while they were 2941 and 816 at b-value of 3000 s/mm^2, respectively. Figure 5 presents a qualitative comparison.

Figure 6 compares the gold standard estimates from PAS to the individual estimates from Q-ball and vice versa. SF follows the same trend for all four scenarios for the single fiber population. For

the single fiber case, SF is higher when the PAS treated as the baseline (red curves: Figure 6A vs 6C and Figure 6B vs. 6D). Yet, for the two-fiber model, Q-ball ground truth generally agrees with PAS at high b-value (>0.5), but a substantial fraction (~80%) of PAS two-fiber cases are not seen in Q-ball (black curves: Figure 6A vs 6C and Figure 6B vs. 6D). The three fiber cases are not consistent for either baseline or b-value scenario (blue curves: Figure 6). We can appreciate these levels of agreement qualitatively in Figure 7. The major white matter tracts have single fiber detected and have high SF with both approaches used as gold standards (Figure 7 first column). The impact of the number of voxels shown with two fibers on the overall SF is shown in the second column of Figure 7.
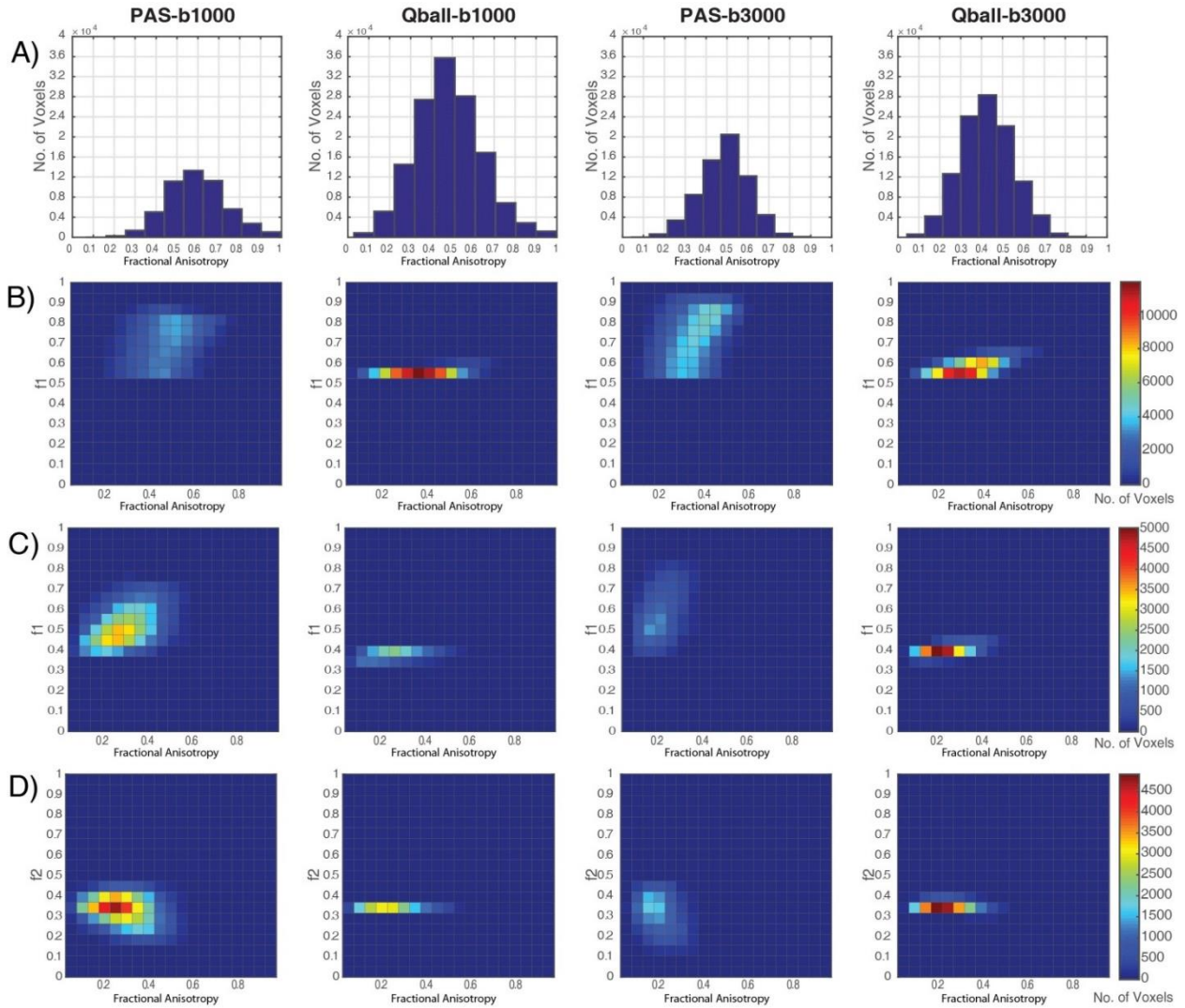
Figure 3: Peak Fractions of the methods across eleven single scans per b-values of 1000 s/mm² and 3000 s/mm². A) Number of voxels mapped as a function of FA. B) Two fiber population f1 as function of FA with number of voxels as the third dimension. C) Three fiber population f1 as function of FA with number of voxels as the third dimension. D) Three fiber population f2 as function of FA with number of voxels as the third dimension.

Chapter 5

Discussion

In the literature, Q-ball has been shown to detect crossing angles in multi-fiber regions down to 45 degrees at b-values of 8000 s/mm^2. Given sufficient SNR using high quality phantom data, and Q-ball improves on accuracy with b-values > 4000 s/mm^2 [12]. Typically, these b-values are not clinically feasible. Crossing fiber angles have been detected with Q-ball for FA less than 0.4 [11]. Meanwhile, PAS resolves greater crossing fiber populations on sparse diffusion data and is able to resolve crossing fibers at lower b-values which are clinically feasible [10].

Herein, we find that both the methods perform well when self-comparing each single scan with concatenated multiple single scans (gold standard model). In terms of inter-model comparison there is little agreement which is suggestive of two different types of underlying global micro-architecture of the human brain. Specifically, both methods work well on single fiber population scenarios (however, this is not the application for which the methods were designed to address) (Figure 2) [1, 7]. However, Q-ball performs better than PAS for single fiber scenarios, which is interesting because it is probable that PAS is detecting false positives. Comparing (Figure 2 & Figure 4) we see that specifically for lower FA there is high standard deviation which is indicative of the false positives for PAS. Q-ball performs consistently for this scenario.

With the evaluated imaging sequences, Q-ball and PAS reliably detect multiple fibers only for crossing regions with no more than two fiber populations (Figure 2). Note that PAS and Q-ball both show low reproducibility for extreme FA values which is a likely artifact. The inference is that the detection of fiber population might not be accurate. At high values of FA it is more probable that single fiber populations would be expected rather than two fiber populations. While the lower FA regions show disagreement for two fiber populations which is not as extreme as for higher FA values. Suggestively it could be noise that is making the methods underperform in those regions. It is also possible that the methods are not able to resolve more complex architecture, which might be present in the lower anisotropic regions as there is evidence of very low reproducibility in three fiber populations regions or more. Comparison with histological validation

may indicate which methods are more accurate in regions of disagreement [27, 28]. It is likely that usage of these voxels might lead to spurious tracts or false continuations.
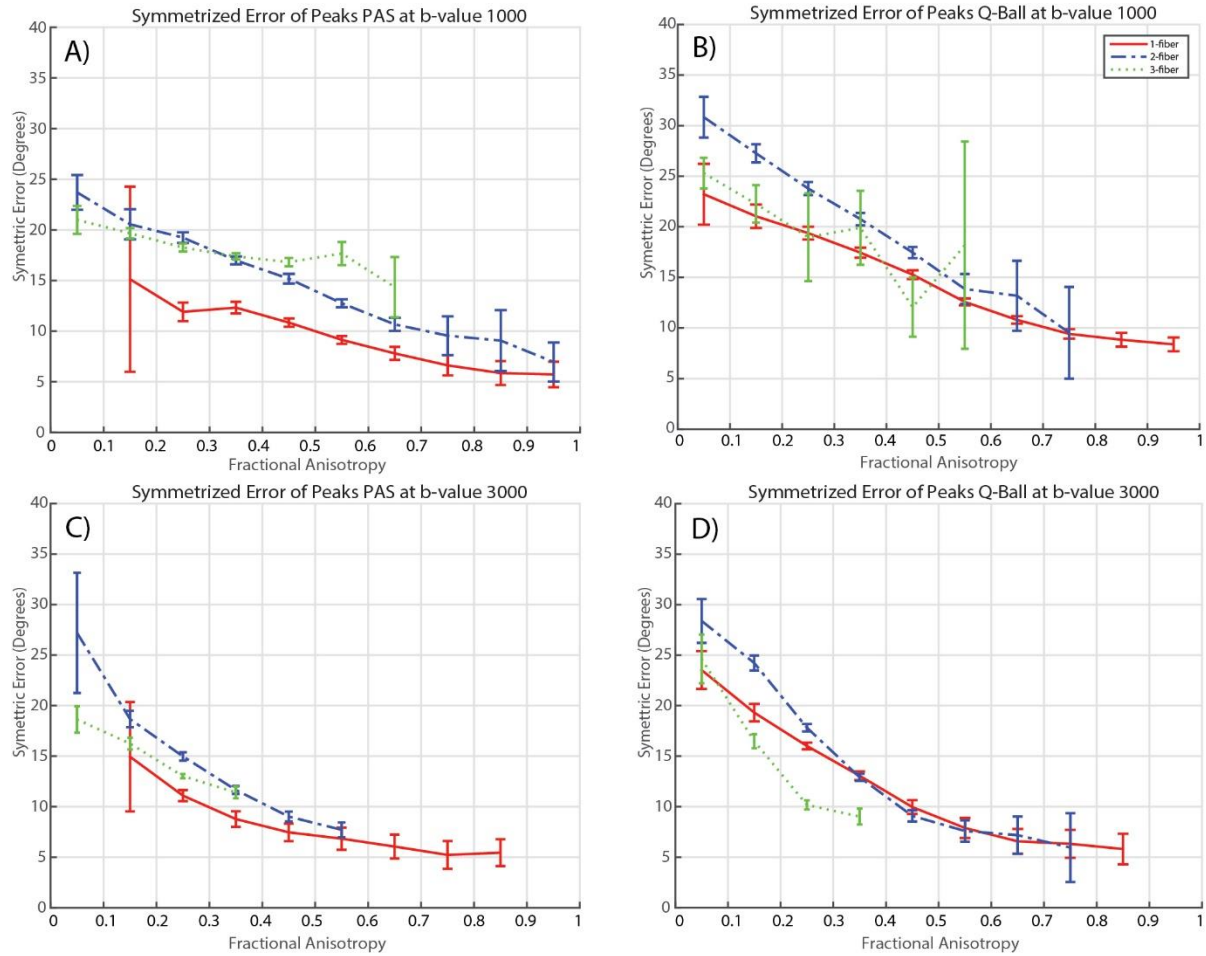

Figure 4: Symmetric angular error is shown for A) PAS at b-value of 1000 s/mm^2, B) Q-ball at b-value of 1000 s/mm^2, C) PAS at b-value of 3000 s/mm^2, and D) Q-ball at b-value of 3000 s/mm^2.

Comparing (Figure 2) and (Figure 4), we find an interesting difference. The symmetric angular error (Figure 4) shows that most of the errors detected for three fiber populations are less than the two-fiber population scenario. Yet this is contradicted by the SF (Figure 2) which shows us that there is hardly any agreement for three fiber scenarios. Though our analysis suggests that they are not reproducible there might be a possibility to improve them and increase their reproducibility. Robust fitting of HARDI methods with removal of outlier volumes could lead to improvements.

The peak fractions of Q-ball show a self-consistent, but distinct, value in most scenarios (Figure 3). While PAS shows them consistently as well but across a wider range. It can be expected from Q-ball that they will be consistent values because a smooth function (ODF) has been normalized. While PAS is a spikier function and hence the wider range of fiber fraction. Characterization of the reconstruction of PAS and ODF may lead to a better understanding but it is beyond the scope of this article which deals with fiber population and their angular error. A deeper understanding of the differences between ODF and FOD methods are needed, in particular peak fractions lead to quite different interpretations for the different approaches. This is not surprising as the ODF function is quite smooth and not intended to directly model the fiber fraction. For typical clinical b-values (~1000 s/mm^2) for PAS offers advantages for sensitivity and reproducibility. Q-ball can achieve similar reproducibility performance as PAS given moderate increases in SNR or directions [12]. For higher b-values, Q-ball has some advantages (Figure 3) and (Figure 4), but PAS appears to be a more reasonable choice given higher reproducibility of crossing fiber majorly of the two fiber populations (Figure 2) and (Figure 4). However, care should be taken in interpretation of both methods as to which regions they are applied as both methods are unstable at the extreme of FA (Figure 2).
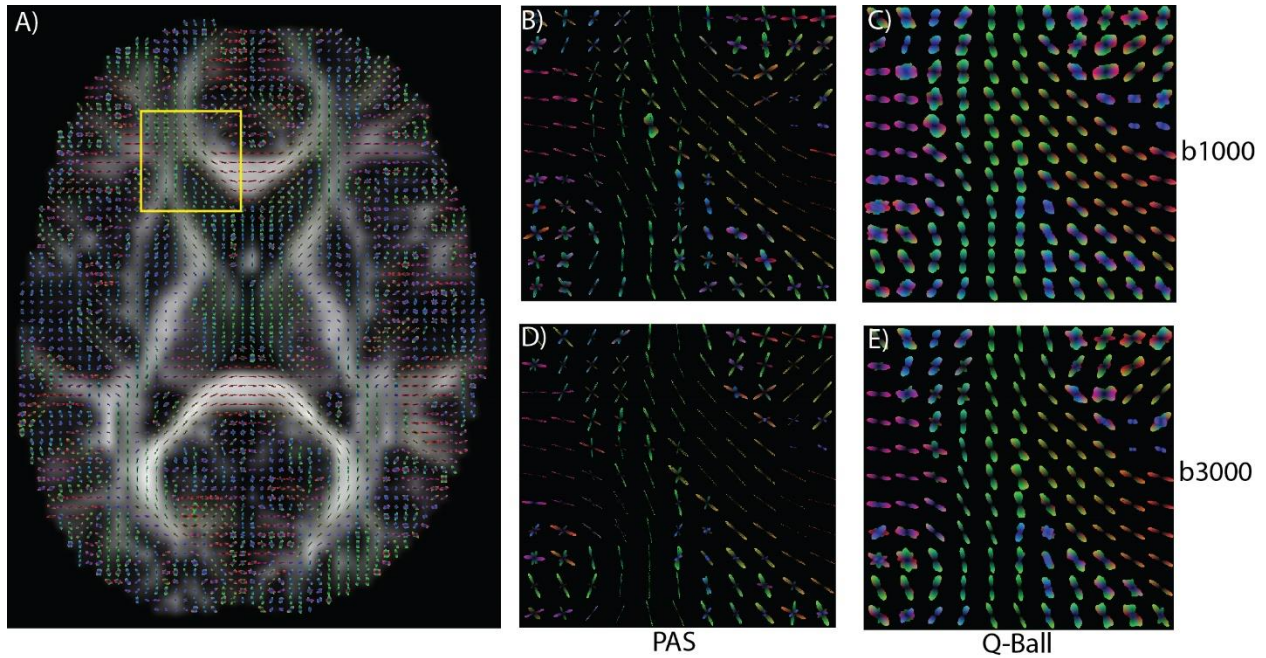
Figure 5: A) Q-ball is shown for the middle axial slice at b-value of 3000 s/mm^2. Enlargements are presented for: B) PAS at b-value 1000 s/mm^2, C) Q-ball at b-value 1000 s/mm^2, D) PAS at b-value 3000 s/mm^2, and E) Q-ball at b-value 3000 s/mm^2

Prior conference analysis of the data, showed that PAS resolves crossing fibers more consistently than Q-ball at moderate and higher crossing angles. Accuracy and consistency for both Q-ball and PAS have been shown to increase with increasing SNR (our empirical data is low SNR) [8, 12], but the observed methodological effects are not mitigated by large quantities of data as indicated as at the comparison between gold standard models computing using all available data (Figure 2) and (Figure 4). In [8], PAS was consistent in all cases with SNR > 16, but for Q-ball to reach this level of consistent/accuracy SNR >24 (which ours is not, and is not often seen in clinical scans). Note that the SNR of the presented data were 11.828 in the centrum semiovale (WM), in the peripheral white matter, and 5.838 in the cortical gray matter in the B0 images. PAS accuracy and consistency is better than Q-ball for crossing fibers at our low/clinically feasible SNR regime, Q-ball is more consistent than PAS in single fiber regions at a lower SNR. This is interesting to note, probably due to the false positives in PAS.

At extreme values of FA there is noticeable disagreement between Q-ball and PAS even for the two-fiber case (Figure 6 and Figure 7). High FA would appear to indicate a single fiber population,

so multiple fibers in these regions could be justified as false positives, while low FA would lean toward a predisposition for complex fiber structure, but limited reproducibility would lead one to justify as a lack of specificity.

In summary, the analyses for *single-fiber populations* are in good self-agreement with PAS, however there is the possibility of false positives. Q-ball performs qualitatively better with fair inter-model agreement. For *two-fiber populations*, the methods are in fair self-agreement except for extreme high or low FA regions. Overall PAS shows more reproducibility and the inter-model agreement is reasonable for mid-ranges of white matter FA ($0.4 <$ FA < 0.6). The *three-fiber population case* shows low self-agreement indicating model instability for both PAS and Q-ball. There is little agreement between both the methods in terms of crossing fibers (Figure 6, 7). Visually also the agreement is less than expected given crossing fiber regions or two and more fiber population voxels. Both the methods clearly suggest two different fundamental micro-architecture of the human brain and they agree in very few regions.
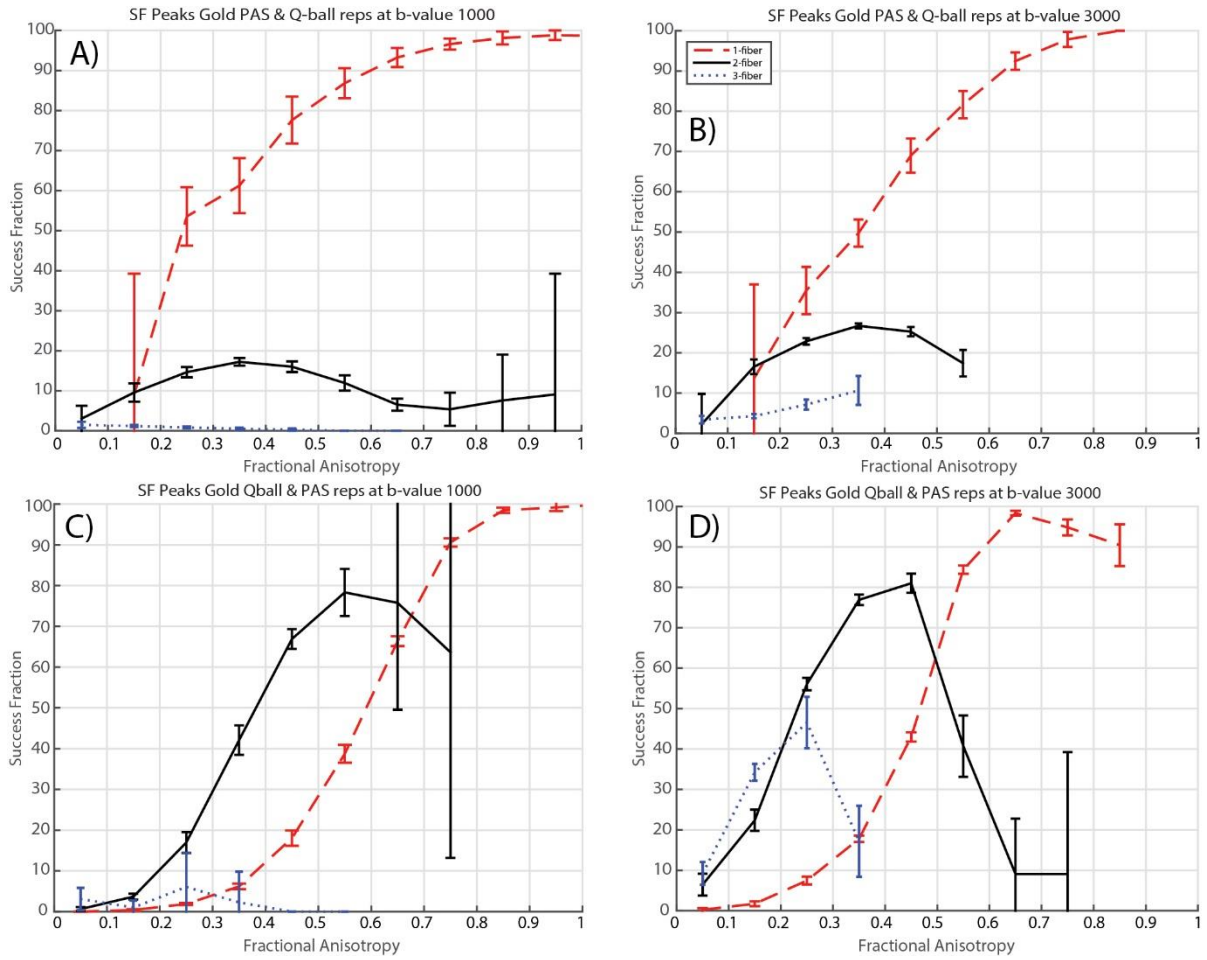
Figure 6: A) SF gold standard model PAS and test models Q-ball at b-value of 1000 s/mm^2. B) SF gold standard model PAS and test models Q-ball at b-value of 3000 s/mm^2. C) SF gold standard model Q-ball and test models PAS at b-value of 1000 s/mm^2. D) SF gold standard model Q-ball and test models PAS at b-value of 3000 s/mm^2.
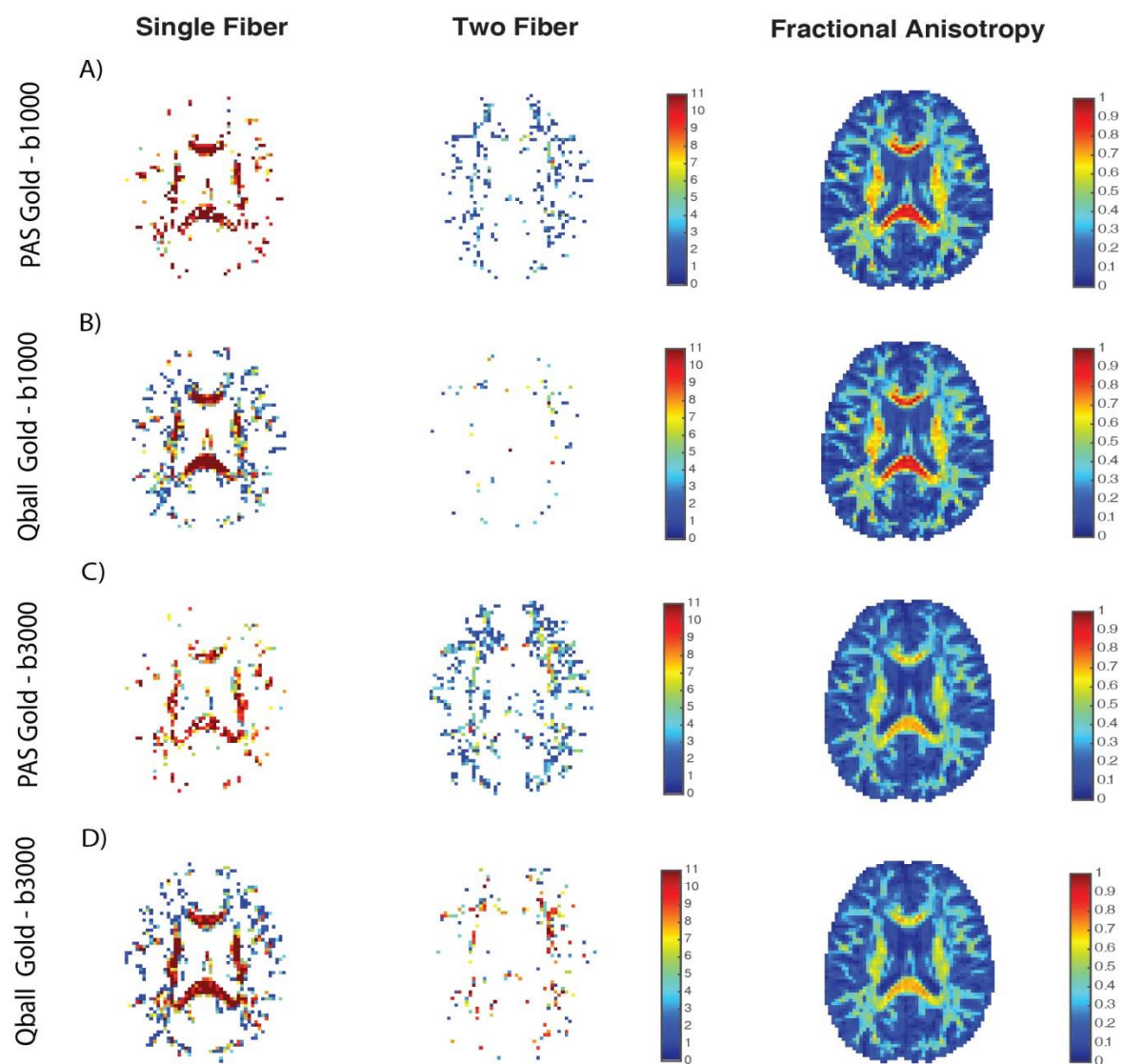
Figure 7: Middle-axial slice spatial map for inter-model comparison. A) PAS gold standard model and Q-ball test models at b-value 1000 s/mm^2. B) Q-ball gold standard model and PAS test models at b-value 1000 s/mm^2. C) PAS gold standard model and Q-ball test models at b-value 3000 s/mm^2. D) Q-ball gold standard model and PAS test models at b-value 3000 s/mm^2.

References

Basser, P.J., J. Mattiello, and D. LeBihan, *Estimation of the effective self-diffusion tensor from the NMR spin echo.* Journal of Magnetic Resonance, Series B, 1994. **103**(3): p. 247-254.

2.   Özarslan, E., et al., *Resolution of complex tissue microarchitecture using the diffusion orientation transform (DOT).* Neuroimage, 2006. **31**(3): p. 1086-1103.

3.   Anderson, A.W., *Measurement of fiber orientation distributions using high angular resolution diffusion imaging.* Magnetic resonance in medicine, 2005. **54**(5): p. 1194-1206.

4.   Tournier, J.-D., et al., *Direct estimation of the fiber orientation density function from diffusion-weighted MRI data using spherical deconvolution.* Neuroimage, 2004. **23**(3): p. 1176-1185.

5.   Jansons, K.M. and D.C. Alexander, *Persistent angular structure: new insights from diffusion magnetic resonance imaging data.* Inverse problems, 2003. **19**(5): p. 1031.

6.   Tuch, D.S., *Q‑ball imaging.* Magnetic resonance in medicine, 2004. **52**(6): p. 1358-1372.

7.   Farrell, J.A., et al., *Effects of signal‑to‑noise ratio on the accuracy and reproducibility of diffusion tensor imaging–derived fractional anisotropy, mean diffusivity, and principal eigenvector measurements at 1.5 T.* Journal of Magnetic Resonance Imaging, 2007. **26**(3): p. 756-767.

8.   Sweet, A. and D. Alexander. *Reduced encoding persistent angular structure*. in *International society for magnetic resonance in medicine*. 2010.

9.   Descoteaux, M., et al., *Regularized, fast, and robust analytical Q‑ball imaging.* Magnetic resonance in medicine, 2007. **58**(3): p. 497-510.

10.   Alexander, D. *A comparison of q-ball and PASMRI on sparse diffusion MRI data*. in *Proc. Int. Soc. Magn. Res. Med*. 2004.

11.   Gorczewski, K., S. Mang, and U. Klose, *Reproducibility and consistency of evaluation techniques for HARDI data.* Magnetic Resonance Materials in Physics, Biology and Medicine, 2009. **22**(1): p. 63-70.

12.   Cho, K.-H., et al., *Evaluation of the accuracy and angular resolution of q-ball imaging.* Neuroimage, 2008. **42**(1): p. 262-271.

13. Andersson, J.L., S. Skare, and J. Ashburner, *How to correct susceptibility distortions in spin-echo echo-planar images: application to diffusion tensor imaging.* Neuroimage, 2003. **20**(2): p. 870-888.

14. Andersson, J.L. and S.N. Sotiropoulos, *Non-parametric representation and prediction of single-and multi-shell diffusion-weighted MRI data using Gaussian processes.* Neuroimage, 2015. **122**: p. 166-176.

15. Jenkinson, M. and S. Smith, *A global optimisation method for robust affine registration of brain images.* Medical image analysis, 2001. **5**(2): p. 143-156.

16. Holmes, C.J., et al., *Enhancement of MR images using registration for signal averaging.* Journal of computer assisted tomography, 1998. **22**(2): p. 324-333.

17. Tustison, N.J., et al., *N4ITK: improved N3 bias correction.* IEEE transactions on medical imaging, 2010. **29**(6): p. 1310-1320.

18. Avants, B.B., N. Tustison, and G. Song, *Advanced normalization tools (ANTS).* Insight J, 2009. **2**: p. 1-35.

19. Avants, B.B., et al., *Symmetric diffeomorphic image registration with cross-correlation: evaluating automated labeling of elderly and neurodegenerative brain.* Medical image analysis, 2008. **12**(1): p. 26-41.

20. Asman, A.J. and B.A. Landman, *Formulating spatially varying performance in the statistical fusion framework.* IEEE transactions on medical imaging, 2012. **31**(6): p. 1326-1336.

21. Asman, A.J. and B.A. Landman, *Non-local statistical label fusion for multi-atlas segmentation.* Medical image analysis, 2013. **17**(2): p. 194-208.

22. Freund, Y. and R.E. Schapire. *A desicion-theoretic generalization of on-line learning and an application to boosting*. in *European conference on computational learning theory*. 1995. Springer.

23. Klein, A., et al. *Open labels: online feedback for a public resource of manually labeled brain images*. in *16th Annual Meeting for the Organization of Human Brain Mapping*. 2010.

24. Cook, P., et al. *Camino: open-source diffusion-MRI reconstruction and processing*. in *14th scientific meeting of the international society for magnetic resonance in medicine*. 2006. Seattle WA, USA.

25. Cook, P.A., et al., *Camino: Diffusion MRI reconstruction and processing.* Cetre for Medical Image Computing, Department of Computer Science, University College London, UK, 2005.

26.   Alexander, D.C. *Maximum entropy spherical deconvolution for diffusion MRI*. in *Information Processing in Medical Imaging*. 2005. Springer Berlin Heidelberg.

27.   Schilling, K., et al., *Reproducibility and variation of diffusion measures in the squirrel monkey brain, in vivo and ex vivo.* Magnetic resonance imaging, 2017. **35**: p. 29-38.

28.   Schilling, K., et al., *Comparison of 3D orientation distribution functions measured with confocal microscopy and diffusion MRI.* Neuroimage, 2016. **129**: p. 185-197.